J. Phys. Chem. A **2007,** *111,* 6813−6821

Photoelectron Imaging of Atomic Iodine Following A-Band Photolysis of CH_3I[†]

Changjin Hu,[‡] Shixin Pei,[‡,§] Yi-Li Chen,[‡,||] and Kopin Liu*[,‡,||]

Institute of Atomic and Molecular Sciences (IAMS), Academia Sinica, P.O. Box 23-166, Taipei, Taiwan 10617, Institute of Mathematics and Physics, Nanjing University of Information Science and Technology, Nanjing 210044, China, and Department of Chemistry, National Taiwan University, Taipei, Taiwan 10617

Received: January 14, 2007; In Final Form: March 1, 2007

Photoionization of the iodine atom following methyl iodide A-band photodissociation was studied over the wavelength range of 245.5−261.6 nm by photoelectron imaging technique. Final state-specific speed and angular distributions of the photoelectron were recorded. Two types of the photoelectron resulted from ionizing the I atom from the photodissociation of CH_3I were identified: (a) (2 + 1) REMPI of the ground state I atom, and (b) two-photon excitation of spin−orbit excited $I(^2P_{1/2})$ to autoionizing resonances converging to the $^3P_1$ state of I^+. In addition, some weaker signals were attributed to one-photon ionization of I atoms produced in some higher excited states from multiphoton ionization of CH_3I followed by dissociation. Analysis of relative branching ratios to different levels of I^+ (in case a) revealed that the final ion level distributions are generally dominated by the preservation of the ion-core configuration of the intermediate resonant state. A qualitative interpretation of the electron angular distribution from an autoionization process is also given.

I. Introduction

The A-band photolysis of methyl iodide (CH_3I) is a prototypical system for studying molecular photodissociation dynamics, and has attracted much attention both experimentally and theoretically over the past decades.[1−4] The well-known A-band of CH_3I, lying in the range of 210−330 nm with the maximum near 260 nm and comprising three dissociative excited electronic states (designated as $^3Q_0$, $^3Q_1$, and $^1Q_1$ by Mulliken[5]), corresponds to the excitation of a nonbonding 5pπ iodine electron to the σ* antibonding C−I orbital.[6] Photoexcitation to the A-band results in rapid direct dissociation producing CH_3 and $I(^2P_{3/2}$ and $^2P_{1/2})$ on a time scale of ∼150 fs from a real-time measurement.[7]

With the availability of high power pulsed lasers, the competition between the multiphoton ionization (MPI) and dissociation processes of CH_3I in the wavelength region 266−307 nm has also been investigated and clarified, using a two-color, time-of-flight mass spectrometric technique.[8] It was shown that the predominant ion is I^+ from the MPI of the neutral I-atom. Recognizing that the fragmentation of CH_3I can be an excellent source of both iodine atom and methyl radical for spectroscopic studies, numerous Rydberg states of iodine have been identified in this way by Pratt using photoelectron spectroscopy[9] or from MPI spectrum of atomic iodine.[10] From the pulsed-field extracted two-photon threshold photoionization spectrum of CH_3I in the region from 255 to 230 nm, two other Rydberg series of atomic iodine, $(^3P_1)np$ and $(^3P_1)nf$, have also been assigned to the autoionizing resonances by Zhu and Grant.[11] In addition, Jung and co-workers have studied (2 + 1) REMPI of atomic iodine in the wavelength region 277−313 nm using photoelectron imaging technique.[12] Both relative branching ratios to the final levels of I^+ (in $^3P_2$, $^3P_{0,1}$, $^1D_2$ and $^1S_0$) and the angular distributions of outgoing photoelectrons were obtained. It was found that the final ion level distributions are dominated by the preservation of the ion-core configuration of resonant excited-state defined by the $J_c l$ coupling scheme.

Bondybey and co-workers proposed in a series of reports[13−16] a new probe to watch how a photoexcited molecule dissociates using a nanosecond laser. The idea is analogous to the Raman emission probe pioneered by Kinsey and co-workers over two decades ago,[3] and can be outlined as follows. When a molecule is photoexcited to a repulsive potential energy surface, the molecule undergoes a rapid bond rupture with a near unity dissociation yield. Nonetheless, a very tiny fraction of dissociating molecule can emit photon—the resonance Raman emission, which carries unique imprints of short-time dynamics of the photodissociation process. Since the photoelectron spectroscopy in general has less restricted selection rules than a Raman process, it potentially affords the opportunity to probe more vibrational modes that are active while the photofragments are flying part. Bondybey' group carried out exactly such a experiment by acquiring the one-color, two-photon zero kinetic energy (ZEKE) spectra of CH_3I via the intermediate A-band.[13−16] The short-time dissociation dynamics is manifested as a series of vibrationally assignable peaks of the molecular ion CH_3I^+, which was interpreted as the projection of the dissociating wavepacket onto the ionization continuum—rather than back onto the neutral ground state in the Raman emission approach—by absorbing another photon from the repulsive surface.

Motivated by these reports, we recently engaged a project to explore the idea further by using the photoelectron imaging technique in a two-color, two-photon experiment. During the course of that study, many photoelectron images of the I-atom fragments were also taken, which served as a convenient reference system for rigorous calibration of the photoelectron imaging apparatus (in both speed and angle) due to the well-known energetics. In addition, this set of images revealed interesting photoionization dynamics, which is the main subject of this report.

[†] Part of the special issue "M. C. Lin Festschrift".

* Corresponding author.

[‡] IAMS.

[§] Nanjing University of Information Science and Technology.

[||] National Taiwan University.

10.1021/jp070298g CCC: \$37.00

II. Experimental Section

The experimental apparatus used in this study is similar in spirit to the time-sliced velocity-map imaging setup described elsewhere.[17,18] However, several minor, yet crucial modifications were made to our original slice-imaging setup in order to achieve higher quality photoelectron image for the present experiment. Briefly, a cold molecular beam was produced by expanding a gas mixture, which was prepared by bubbling He through liquid CH_3I at 274K (to suppress the I_2 contamination) with typical about 9.5% CH_3I in He at total pressure of 30 psi, into the source chamber via an Even-Lavie valve (pulse duration of 30μs, and with 0.5 mm nozzle diameter). The molecular beam, which was skimmed and collimated to ~1 mm diameter along the ion time-of-flight axis, was intersected at right angles by a frequency-doubled laser beam generated by a Nd:YAG pumped dye laser. The same laser was used for the A-band excitation of CH_3I and subsequent ionization of either the parent molecule or the neutral photofragments (mainly I-atoms in this study) in a one-color experiment. The laser was vertically polarized (i.e., parallel to the detector face) and focused by a $f = 50$ cm spherical lens to the center between the repeller and extractor electrodes.

Electrons or ions produced in the interaction region were velocity-imaged by a suitable electric field and impacted onto the Chevron-type microchannel plate (MCP) after passing through a 45 cm field-free region. The fluorescence from a P46-phosphor was captured by a CCD camera and transferred to a computer on every-shot basis for event counting and for further data analysis. Two modifications of the apparatus were made to reduce the spurious photoelectron background. First, a turbo pump replaced the diffusion pump for the source chamber. Second, in view of the difficulty in time-slicing the photoelectron cloud, a simplified ion-optics assembly with significantly tighter focus and more restricted field-of-view than the original setup[17,18] was adapted for the conventional "crushed" velocity imaging.[1,2] The new setup consists of five thin electrodes (repeller, extractor, and three lenses) with the openings, in order of 10 mm, 10 mm, 20, 60, and 60 mm respectively. The spacing between the successive electrodes was kept at 19 mm. The voltage ratio for this arrangement was maintained, although the voltage employed for the repeller (V_R) was changed over the range of 900−5000V, depending on the kinetic energy release of photoelectrons. A double-layered μ-metal shield (0.5 mm thickness each) was added to the whole ion optics assembly to minimize the effects from the earth's magnetic field.

As mentioned in the Introduction, the present study also serves as a calibration, both in speed and angle, of photoelectron imaging detector. From the well-documented energy levels of I-atom and I^+-ion, the speed calibration factor (i.e., km/sec per pixel) is readily obtained from the consistent assignments of the image features. The angular calibration is, on the other hand, more problematic and often neglected in literatures by simply symmetrizing the raw image prior to data analysis. Even with event-counting technique, we found that the residual nonuniformity of the detection sensitivity still manifests itself as slight asymmetry in angular distributions, which could lead to some errors in the reported β values. Hence, considerable efforts were devoted to finding a way to remedy the angular asymmetry problem.

An ideal source for calibrating the angular variations in detection sensitivity will be an isotropic and uniform distribution. We generated such a source by first choosing a nearly isotropic single-ring image at $\lambda = 244.106$ nm and then rotating the laser polarization 90° (i.e., along the TOF axis) to acquire the "calibration" image. Owing to the symmetry properties of the photoionization process, such a "calibration" image is necessarily uniform and thus serves the purpose for angular calibration of the detector sensitivity.

Figure 1 illustrates the effects of the nonuniform sensitivity on the measured angular distribution. The corresponding photoelectron image is the peak number 21, whose peak position is labeled in Figure 2 and the raw image shown in Figure 5 (vide infra). To perform quantitative analysis of the image asymmetry, we took the four quadrants of the photoelectron image and analyzed them independently. Thus, a raw image was converted to four symmetrized images prior to the inversion transformation. The resulted angular variations of the raw image data are presented in Figure 1a,b in the Cartesian and the polar representations, respectively. Noticeable angular asymmetry is vividly displayed. The same raw image was then corrected for the nonuniform sensitivity, using the "calibration" image, and analyzed similarly. The "corrected" results are shown in Figure 1c,d for comparisons. A significant improvement, through not perfect, can clearly be seen. The lines in Figure 1a,c are the best-fitted distributions for the data in each individual quadrant of Figure 1c,; while the line in Figure 1b,d is the best fit after symmetrizing the "corrected" image (though the actual data points shown in panel d remained unsymmetrized). We found that after correcting the detector sensitivity variations, the best-fitted β-coefficients for a "corrected", symmertrized image are well within the standard deviations of the β-coefficients obtained from the unsymmetrized four quadrants of the same "corrected" image. This is also clearly illustrated in panel d by comparing the goodness of the line-fit to the actual data point. Hence, for the results to be presented below, the data points are from the symmetrized, angular-corrected images and the best-fitted β coefficients are the averaged results from analyzing the four quadrants.

III. Results and Discussion

A. Spectral Assignment of MPI of Atomic Iodine. Presented in Figure 2 are the three (one-color) spectra over the two-photon energy range of 76 500−81 200 cm^{-1}: the photoelectron spectrum (a), the photoionization yield spectrum of the parent molecular CH_3I (b), and the I^+ cation-detected photoionization following the photodissociation of CH_3I (c). Over most of the wavelength region of this study, two-photon energy is sufficient to ionize the parent molecule CH_3I (ionization potential, IP $= 76\,932 \pm 5$ cm^{-1});[16] indeed, the onset of the photoionization of CH_3I can be observed as a clear step in Figure 2a,b But the spectral features in Figure 2b cannot be assigned as the $CH_3I(\tilde{X}^1A_1) \rightarrow CH_3I^+(\tilde{X}^+\ ^2E_{3/2})$ resonant transitions, which has been observed in threshold photoionization spectroscopy.[16] Instead, they are ascribed to the transitions from the ground state to the superexcited (or autoionizing) states of CH_3I, as will be shown in the future. Interestingly, the I^+ cation-detected photoionziation spectrum, shown in Figure 2 c, appears nearly identical to the ZEKE spectrum of Zhu and Grant[11] and can be assigned to the resonant photoionization of the fragmented iodine atoms. Since the photoelectron detection here did not differentiate the photoelectron produced from the ionization of either the parent molecule CH_3I or the fragmented iodine atom, the features in the photoelectron spectrum, Figure 2a, comprise spectral features from both sources. Their relative intensities depend on the laser intensity used because of different numbers of photon involved: a two-photon process for $CH_3I \rightarrow CH_3I^+ + e^-$, whereas at least three photons are required for $CH_3I \rightarrow CH_3 + I \rightarrow I^+ + e^-$.

In this study, we focused on the photoionization dynamics of the iodine atom by photoelectron imaging technique. A total

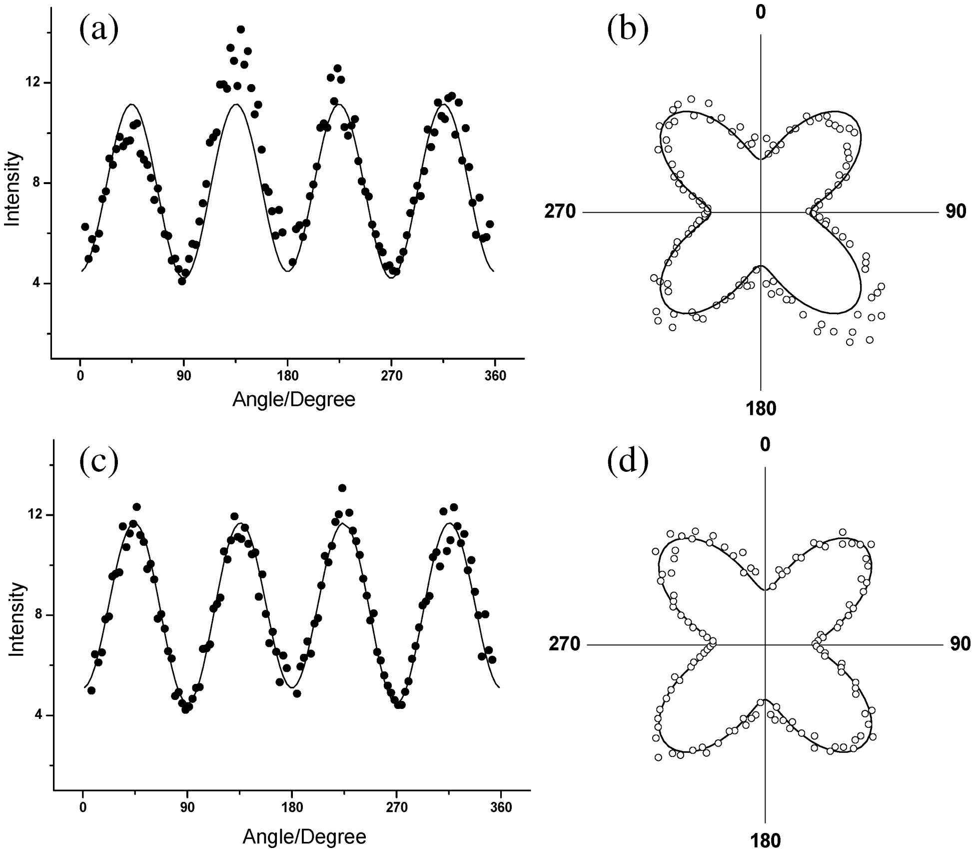

Figure 1. An illustration of the effects and the correction of the angular asymmetry of the photoelectron image. The laser polarization is vertical. Shown in panels a and b are the results from a raw image and panels c and d the results from the “corrected” image, using a “calibration” image. A significant improvement is clearly seen in panels c and d. The residual, slight asymmetry probably arises from the statistical variations of the “calibration” image. See text for details.

of twenty-one spectral features, which are labeled in Figure 2a,c in sequence, were imaged. The spectral positions and assignments, as well as the peak widths, are summarized in Table 1. Two different types of spectral features are classified in Table 1. One class shows narrow peaks with a typical width of <1 cm$^{-1,}$; and its formation is ascribed to (2 + 1) REMPI process of predominantly the ground state I($^2P_{3/2}$). The observed widths are mainly due to the dye laser scan rate and the Doppler broadening of the I($^2P_{3/2}$) fragments from photodissociation. Thus, the overall processes can be expressed as

$$\begin{gathered} \mathrm{CH_3I} + h\nu \rightarrow \mathrm{CH_3} + \mathrm{I}(^2\mathrm{P}_{3/2}) \\ \mathrm{I}(^2\mathrm{P}_{3/2}) + 2\,h\nu \rightarrow \mathrm{I}^* \\ \mathrm{I}^* + h\nu \rightarrow \mathrm{I}^+ + \mathrm{e}^- \end{gathered} \tag{1}$$

The other type exhibits a broader wider peak with typical fwhm in the order of 2−15 cm^{-1}. As will be shown later, those peaks are assigned to two-photon transitions originating from the spin−orbit excited state I($^2P_{1/2}$) and terminating in superexcited Rydberg states converging to the I$^+$($^3P_1$) ionization threshold.[11] In other words, the processes involved are

$$\begin{gathered} \mathrm{CH_3I} + h\nu \rightarrow \mathrm{CH_3} + \mathrm{I}(^2\mathrm{P}_{1/2}) \\ \mathrm{I}(^2\mathrm{P}_{1/2}) + 2\,h\nu \rightarrow [\mathrm{I}^{**}] \rightarrow \mathrm{I}^+(^3\mathrm{P}_2) + \mathrm{e}^- \end{gathered} \tag{2}$$

where [I**] denotes a superexcited state that decays through autoionization process with a lifetime inversely proportional to its peak width. Two-photon excitation of a *p*-orbital electron dictates the superexcited Rydberg states being of the *p*- and *f*-series due to the optical selection rule $\Delta l = 0$ and 2. Both the intermediate excited states in eq 1 and the superexcited states in eq 2 of neutral iodine are described as J_cl coupling in Table 1, as originally suggested by Minnhagen.[19] In this coupling scheme, the total angular momentum J_c of the I$^+$ ion core is coupled to the orbital angular momentum l of the Rydberg electron to give the resultant K. The spin, s, of the Rydberg electron is then coupled to K to give the total angular momentum J. The states are then labeled as ($^3P_{Jc}$)$nl[K]_J$, where ($^3P_{Jc}$) describes the ion core.

In general, the transition energies reported in Table 1 for the (2 + 1) REMPI process 1 are about 1 cm^{-1} larger than the Minnhagen’s values.[19] Previously, two series of autoionzing states, ($^3P_1$)*np* and ($^3P_1$)*nf*, have been identified by Zhu and Grant, using one-color two-photon ZEKE spectroscopic technique, with quantum defects of ∼0.45 and ∼0.045 respectively.[11] Although the reported transition energies[11] appear to be systematically smaller than this work for process 2 by about 4−6 cm^{-1}, the spectral assignments are entirely consistent in view of the expected offset by the delayed field technique. A few points are, however, worth noting here.

First, it is known[9] that effective principal quantum number n* can be calculated directly from the expression

$$n^* = [R_I/(E(^3P_1) - E_{nl})]^{1/2} \tag{3}$$

where R_I is the Rydberg constant for iodine (109736.85 cm^{-1}), E($^3P_1$) is the $^3P_1$ ionization energy, and E_{nl} the observed energy of the Rydberg state with respect to the ground state I($^2P_{3/2}$). From eq 3, n^* is about 2.5 for 5s^{2}5p^{4}6p configuration, 3.5 for 5s^{2}5p^{4}7p, and 4.526 for the Rydberg states previously

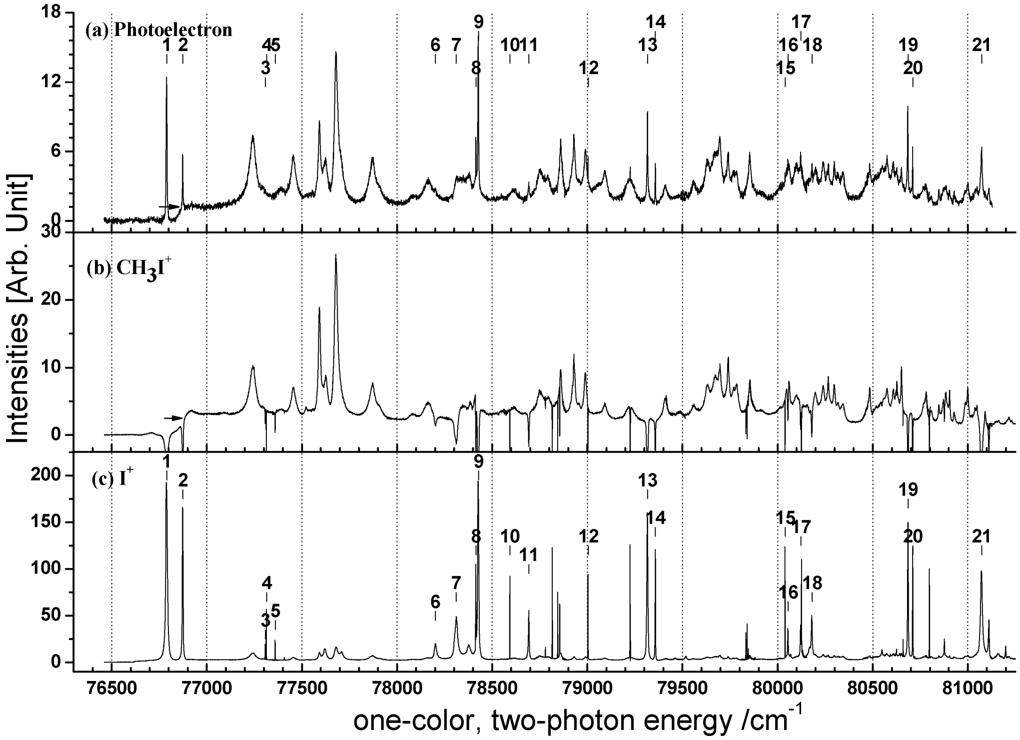

Figure 2. Comparison of the photoelectron spectrum (a), with the two-photon ionization spectrum of parent molecule CH_3I (b), and the photoionziation spectrum of the prompt fragment I-atom following the photodissociation of CH_3I (c). The arrows in spectra a and b mark the ionization potential of the parent molecule CH_3I. The negative-going signals in spectrum b is the experimental artifact, arising from the electronics ringing of the huge proceeding mass I^+, as seen in spectrum c, of the TOF mass spectrometer. Photoelectron images are acquired for those peaks labeled by numbers, for which the spectral assignments are given in Table 1.

TABLE 1: Assignments of the Ionizing Resonances of Atomic Iodine and Their Peak Widths

transition mechanism	peak #	wavelength (λ_{vac}, nm)	transition energy (cm^{-1}) this work	transition energy (cm^{-1}) ref	assignment	peak width (cm^{-1})
(2 + 1) REMPI	3	258.704	77308.4	77307.24[a]	$^2\mathrm{P}_{3/2}\rightarrow(^3\mathrm{P}_2)4f[4]_{7/2}$	0.85 ± 0.04
	4	258.683	77314.9	77313.46[a]	$^2\mathrm{P}_{3/2}\rightarrow(^3\mathrm{P}_2)4f[3]_{7/2}$	0.73 ± 0.01
	5	258.530	77360.6	77359.58[a]	$^2\mathrm{P}_{3/2}\rightarrow(^3\mathrm{P}_2)4f[2]_{5/2}$	0.66 ± 0.04
	8	255.049	78416.3	78415.25[a]	$^2\mathrm{P}_{3/2}\rightarrow(^1\mathrm{D}_2)6p[1]_{3/2}$	0.79 ± 0.04
				78411[b]	$^2\mathrm{P}_{1/2}\rightarrow(^3\mathrm{P}_1)5p[1]_{1/2}$	
	10	254.474	78593.6	78592.55[a]	$^2\mathrm{P}_{3/2}\rightarrow(^1\mathrm{D}_2)6p[3]_{5/2}$	1.01 ± 0.00
				78588[b]	$^2\mathrm{P}_{1/2}\rightarrow(^3\mathrm{P}_1)5p[0]_{1/2}$	
	12	253.150	79004.7	79003.61[a]	$^2\mathrm{P}_{3/2}\rightarrow(^1\mathrm{D}_2)6p[3]_{7/2}$	1.84 ± 0.07
	15	249.872	80041.0	80039.82[a]	$^2\mathrm{P}_{3/2}\rightarrow(^1\mathrm{D}_2)6p[2]_{3/2}$	0.90 ± 0.03
autoionization	1	260.450	76790.3	76784[b]	$^2\mathrm{P}_{1/2}\rightarrow(^3\mathrm{P}_1)4f[2]_{3/2,5/2}$	10.09 ± 0.11
	2	260.166	76874.1	76868[b]	$^2\mathrm{P}_{1/2}\rightarrow(^3\mathrm{P}_1)4f[3]_{5/2}$	4.07 ± 0.08
	6	255.747	78202.3		$^2\mathrm{P}_{1/2}\rightarrow(^3\mathrm{P}_1)8p[2]_{5/2}$	12.87 ± 0.29
	7	255.392	78311.1		$^2\mathrm{P}_{1/2}\rightarrow(^3\mathrm{P}_1)8p[1]_{1/2}$	15.41 ± 0.53
	9	255.009	78428.8	78422[b]	$^2\mathrm{P}_{1/2}\rightarrow(^3\mathrm{P}_1)8p[1]_{3/2}$	6.02 ± 0.07
	11	254.152	78693.2		$^2\mathrm{P}_{1/2}\rightarrow(^3\mathrm{P}_1)8p[2]_{3/2}$	4.36 ± 0.11
	13	252.157	79315.8	79311[b]	$^2\mathrm{P}_{1/2}\rightarrow(^3\mathrm{P}_1)5f[2]_{3/2,5/2}$	5.38 ± 0.10
	14	252.021	79358.5	79352[b]	$^2\mathrm{P}_{1/2}\rightarrow(^3\mathrm{P}_1)5f[3]_{5/2}$	2.28 ± 0.05
	16	249.824	80056.5	80052[b]	$^2\mathrm{P}_{1/2}\rightarrow(^3\mathrm{P}_1)9p[2]_{3/2}$	2.74 ± 0 .09
	17	249.619	80122.1	80117[b]	$^2\mathrm{P}_{1/2}\rightarrow(^3\mathrm{P}_1)9p[1]_{1/2}$	3.62 ± 0.10
	18	249.436	80180.9	80176[b]	$^2\mathrm{P}_{1/2}\rightarrow(^3\mathrm{P}_1)9p[0]_{1/2}$	5.02 ± 0.10
	19	247.874	80686.2	80677[b]	$^2\mathrm{P}_{1/2}\rightarrow(^3\mathrm{P}_1)6f[2]_{3/2,5/2}$	3.60 ± 0.08
	20	247.798	80710.9	80677[b]	$^2\mathrm{P}_{1/2}\rightarrow(^3\mathrm{P}_1)6f[3]_{5/2}$	3.60 ± 0.08
	21	246.693	81072.4	81063[b]	$^2\mathrm{P}_{1/2}\rightarrow(^3\mathrm{P}_1)10p[2]_{5/2}$	10.02 ± 0.20

[a] Ref 19. [b] Ref 11.

labeled as $5p[1]_{1/2}$ in ref 11. Following Minnhagen's work,[19] $5s^25p^46p$ and $5s^25p^47p$ are the only two *np* configurations where all levels based on I^+ ($^3P_1$) are below the $^3P_2$ ionization limit. As such, we prefer to assign the $l = 1$ series as ($^3P_1$)*8p* to *14p* in Table 1, rather than as ($^3P_1$)*5p* to *11p* reported in ref 11.

Second, the transitions corresponding to peaks 8 and 10 were previously assigned as $l = 1$ series converging to $I^+(^3P_1)$, i.e., $(^3P_1)5p[1]_{1/2}$ and $(^3P_1)5p[0]_{1/2}$, respectively, on the basis of quantum defects and spin−orbit splitting patterns.[11] As will be shown later, the images acquired at these two peaks are energetically consistent with two-photon resonant, third photon ionization from $I(^2P_{3/2})$. Therefore, the two transitions are reassigned here as (2 + 1) REMPI of $I(^2P_{3/2})$ with the intermediate resonant state being the *6p* Rydberg series converging to $^1D_2$ level of I^+.

Finally, three new transitions—peaks 6, 7, and 11—were observed. They have quantum defects δ, given by the nonintegral part of $(n-n^*)$, of 0.564, 0.520, and 0.354, respectively,

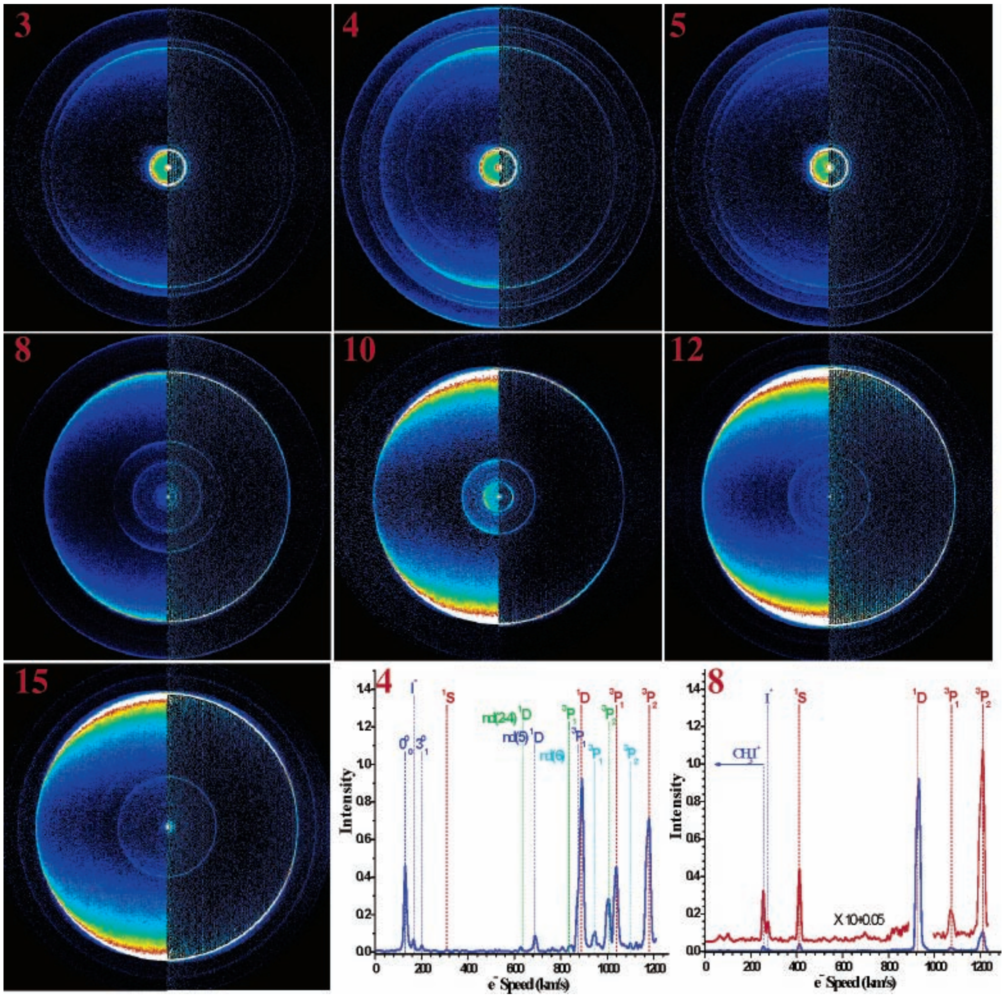

Figure 3. Photoelectron images of the spectral features from the (2 + 1) REMPI processes of the $I(^2P_{3/2})$ fragment. The number marked at the upper-left corner of each panel indicates the peak number, shown in Figure 2, at which the image was acquired. For each panel the left half displays the raw image and the right half shows the inverted one. Exemplified in the bottom are the two representative $P(v_e)$ distributions of the photoelectrons for image numbers 4 and 8, respectively. The assignments of the final ion levels are indicated. The final product branching fractions from all seven images are given in Table 2.

which are about the same magnitude as those of *np* Rydberg series converging to $I^+(^3P_1)$. So, they are tentatively assigned as $(^3P_1)np$ series, as indicated in Table 1.

It is instructive to take a closer look at the peak widths of the autoionizing states, which span from about 2 to 15 cm^{-1}; thus, the corresponding rates of autoionization lie over the range of 0.3−3 ps^{-1}. In addition, the data reveal a systematic trend. For a given autoionizing Rydberg series, i.e., those with the same designation $l[K]_J$, the width decreases monotonically with the increase in n, the principal quantum number of the Rydberg electron. For example, the peak widths for the $nf[2]_{3/2,5/2}$ series decrease from 10 cm^{-1} for $n = 4$ to 5.4 cm^{-1} for $n = 5$ and further down to 3.6 cm^{-1} for $n = 6$, and these variations follow the relationship of $(\mathrm{fwhm})_n \propto n^{-3}$. Similar behaviors are also found for the $nf[3]_{5/2}$, $np[2]_{3/2}$, and $np[1]_{1/2}$ series. This quantitative trend is anticipated and is in accord with the autoionization propensity rules documented by Berkowitz nearly 20 years ago.[20]

B. (2 + 1) REMPI of $I(^2P_{3/2})$. *1. Photoelectron Images and Final Ion State Distributions.* Figure 3 presents seven photoelectron images, arising from the (2 + 1) REMPI process of the $I(^2P_{3/2})$ atom. An extraction voltage $V_R = 4750$ V was used for all images. The peak numbers labeled at the upper-left corner correspond to those shown in Figure 2(c), as well listed in Table 1. The raw image is presented on the left side of each panel, while the reconstructed image, inverted by the basis-set expansion method (BASEX),[21] is displayed on the right. Also exemplified are two photoelectron speed distributions for peaks 4 and 8, respectively.

The speed of photoelectron can be derived from the conservations of energy and momentum

$$v_e = \sqrt{\frac{2(nh\nu + E_0 - E_i)}{m_e(m_e + m_i)/m_i}} \tag{4}$$

where n stands for the numbers of photon involved in the ionization process, $h\nu$ is the photon energy, E_0 the internal energy of photofragment iodine atom with respect to the ground state $I(^2P_{3/2})$, E_i the internal energy of ionic iodine at the ith level, and m_e (m_i) the mass of the electron (ion). The lowest energy configuration of atomic iodine is $[Kr]5s^25p$,[5] which splits into the $^2P_{3/2}$ ground state and the $^2P_{1/2}$ spin-orbital excited-state at 7603.15 cm^{-1}.[19] The removal of an outer electron produces the $[Kr]5s^25p^4$ configuration of I^+, which yields five levels, $^3P_2$, $^3P_0$, $^3P_1$, $^1D_2$, and $^1S_0$ at 84295.1, 90743.0, 91382.1, 98022.3, and 113796.4 cm^{-1}, respectively, above the neutral ground state $^2P_{3/2}$.[19,22] Given those energetics, the dominant peaks in the $P(v_e)$ distributions can be assigned to the final iodine ion levels as indicated. On the other hand, the slow-speed

TABLE 2: Product Branching Fractions among Final Ion Levels Resulting from the (2 + 1) REMPI Processes of the Fragment I(^{2}P$_{3/2}$) Atom[a]

			I(^{2}P$_{1/2}$) (%)	I(^{2}P$_{3/2}$) (%)				
peak #	2*hν* energy (cm^{-1})	intermediate state	I$^+$(^{3}P$_2$)	I$^+$(^{1}S)	I$^+$(^{1}D)	I$^+$(^{3}P$_{0,1}$)	I$^+$(^{3}P$_2$)	total
3	77308.4	(^{3}P$_2$)4*f*[4]$_{7/2}$	5.0 ± 1.3	0	57.3 ± 1.9	3.0 ± 1.5	34.7 ± 2.4	95.0
4	77314.9	(^{3}P$_2$)4*f*[3]$_{7/2}$	2.3 ± 0.4	0	35.9 ± 2.1	20.7 ± 1.8	41.2 ± 1.5	97.8
5	77360.6	(^{3}P$_2$)4*f*[2]$_{5/2}$	5.1 ± 1.0	0	26.6 ± 1.6 (25)	25.8 ± 1.8 (19)	42.4 ± 2.1 (56)	94.8
8	78416.3	(^{1}D$_2$)6*p*[1]$_{3/2}$	0.6 ± 0.1	2.3 ± 0.1 (3)	84.9 ± 4.6 (86)	1.3 ± 0.2 (0)	11.0 ± 1.5 (11)	99.5
10	78593.6	(^{1}D$_2$)6*p*[3]$_{5/2}$	1.1 ± 0.3	0 (0)	96.3 ± 5.4 (100)	1.2 ± 0.3 (0)	1.3 ± 0.5 (0)	98.8
12	79004.7	(^{1}D$_2$)6*p*[3]$_{7/2}$	0	0.4 ± 0.1	98.0 ± 4.3	0.7 ± 0.1	1.0 ± 0.1	100
15	80041.0	(^{1}D$_2$)6*p*[2]$_{3/2}$	0	1.2 ± 0.2	93.2 ± 2.7	4.2 ± 0.3	1.4 ± 0.4	100

[a] The numbers in parentheses for peaks 5, 8, and 10 are from ref 12.

features, i.e., those <300 km/s, originate from the two-photon ionizations of the parent molecule CH_3I and the spin−orbit excited I(^{2}P$_{1/2}$), labeled as I*. The interpretations of those molecular features are beyond the scope of this report, thus will be given in detail elsewhere. Several intriguing and weak series of transitions have also been observed at the peaks 3, 4 and 5. As illustrated in Figure 3 for peak 4, kinetic energy releases suggest that these transitions correspond to one-photon ionization of some high-lying Rydberg states of iodine atom with (^{3}P)-*nd* configuration,[23] presumably arising from multiphoton excitation and dissociation of parent molecular CH_3I. The branching ratios among the final ion levels appear quite irregular for these transitions. More work is warranted.

The branching fractions among final ion levels from process 1 are summarized in Table 2. Intuitively, a two-photon resonant, third-photon ionization process can be regarded as the conventional single-photon ionization of an electron from the intermediate excited level. In the limitation of one-electron direct ionization, the electronic configuration of the ion core of the resonant intermediate state is preserved (i.e., the core-conserving propensity) during the ionization process.[12] In other words, the formation of ionic levels from a (2 + 1) REMPI process will depend on the electronic configuration of the resonant intermediate state. Among the seven observed transitions of (2 + 1) REMPI of I(^{2}P$_{3/2}$) of this study, the intermediate levels for peaks 8, 10, 12, and 15 converge to the I$^+$(^{1}D$_2$) level (see Table 1). For those ionization processes, the branching fractions for the I$^+$(^{1}D$_2$) state are indeed very large, > 85% and even up to 98% for peak 12. Obviously, the core-level conserving propensity accounts for the final ion distribution in those cases, which also confirms that the intermediate levels can be well represented by the $J_c l$ coupling scheme proposed by Minnhagen.[19]

As to the other three levels converging to I$^+$(^{3}P$_2$), however, a rather different behavior (see Table 2) was observed. Although high ^{3}P$_2$ branching fractions (around 40%) are observed, they also show relatively high ^{1}D$_2$ branching fraction and some populations in ^{3}P$_{0,1}$, indicating significant deviation from the simple core-conserving picture. In general, the violation of core-conserving ionization can arise from several factors, including the configuration interaction of the intermediate resonant state with other excited states of different ion cores and the autoionizaing resonances in the continuum.[12] From Table 2, the core-changing ionization occurs at the (^{3}P$_2$)4*f*[4]$_{7/2}$, (^{3}P$_2$)4*f*[3]$_{7/2}$, and (^{3}P$_2$)4*f*[2]$_{5/2}$ resonant states, lying around 77300 cm^{-1}. The (^{3}P$_2$)4*f* configuration has been reported to be perturbed by the (^{1}D$_2$)6*p* configuration,[19] which might account for the high yield of I$^+$(^{1}D) state. Likewise, the formations of ^{3}P$_{0,1}$ suggest possible configuration interactions between (^{3}P$_2$)4*f* and some other configurations having the ^{3}P$_{0,1}$ core.

It is worth pointing out that the photoionization dynamics of three Rydberg states, (^{3}P$_2$)4*f*[2]$_{5/2}$, (^{1}D$_2$)6p[1]$_{3/2}$, and (^{1}D$_2$)6p[3]$_{5/2}$, have also been studied previously.[12] In that study the initial state is I(^{2}*P*$_{1/2}$), rather than the ground-state I(^{2}P$_{3/2}$), yet nearly identical branching fractions to the present work are reported. Both one-color (2 + 1) REMPI experiments invoke the same intermediate resonant state but from different initial states, so the total ionization energies are different. Identical branching fractions among final ion states from the two studies, therefore, provide a strong support for the negligible autoionization effects on the observed core-changing behaviors.

2. Angular Distribution of Ejected Photoelectrons. The photoelectron angular distribution I(θ), as a function of the angle θ between the laser polarization direction and the direction of the ejected electron *k*-vector, reflects the detailed photoionization dynamics. It can be expressed by

$$I(\theta) \propto \sum_{k=0}^{k_{\max}} \beta_{2k} P_{2k}(\cos\theta) \qquad (5)$$

where $k_{\max} = n + 1$ for a $(n + 1)$ REMPI process, $P_{2k}(\cos\theta)$ are the Legendre polynomials of degree 2*k*, and β_{2k}'s are the anisotropy coefficients.[24−26]

Table 3 lists the fitted β coefficients, up to the $P_6(\cos\theta)$ terms, for the present (2 + 1) REMPI process. Two typical angular distributions and fitted results are displayed as polar plots in Figure 4. The others display similar patterns and the analyses are straightforward; thus, they are omitted here (but the β coefficients are listed in Table 3). As can be seen from Table 3, in all cases the β_6 coefficients are negligibly small. In other words, the photoelectron angular distributions are well characterized by $P_2(\cos\theta)$ and $P_4(\cos\theta)$ terms only or $k_{\max} = 2$ that is smaller than 3 for a three-photon process, suggesting additional angular momentum constraints. If only one intermediate *J*-level is invoked in the (2 + 1) REMPI process, the $k_{\max}$ will be constrained by the maximum allowed integers of 2 + 1, $J + 1$, or $l_{\max}$, whichever is the smallest, where $l_{\max}$ is the maximum orbital angular momentum of ejected photoelectrons.[26,27] Since the *J* values for all seven intermediate levels range from 3/2 to 7/2 (Table 3), the resulted $(J + 1)$-restriction cannot account for the observed $k_{\max} = 2$. Hence, the angular momentum constraint is likely limited by $l_{\max}$. Treating process 1 as a direct one-electron ionization from an intermediate excited state, the character of outgoing electrons from *6p* states (peak numbers 8, 10, 12, and 15) will be a mixture of *s* and *d* partial waves due to the selection rule $\Delta l = \pm 1$, which yields $l_{\max} = 2$. And the observed photoelectron angular distribution reflects the interference pattern of the two partial waves. On the other hand, the ejected electrons will be characterized by the *d* and *g*

TABLE 3: Legendre Weighting Coefficients β_{2k} of Photoelectron Angular Distributions for the (2 + 1) REMPI Processes of the Ground State $I(^2P_{3/2})$[a]

		$^1D_2$			$^3P_1$			$^3P_2$		
peak #	intermediate state	β_2	β_4	β_6	β_2	β_4	β_6	β_2	β_4	β_6
3	$(^3P_2)4f[4]_{7/2}$	1.21	0.45	−0.01				0.48	0.43	−0.04
4	$(^3P_2)4f[3]_{7/2}$	1.38	0.54	0.10	0.99	0.45	0.08	1.09	0.64	0.10
5	$(^3P_2)4f[2]_{5/2}$	0.80	0.38	0.03	0.82	0.24	0.07	0.88	0.57	0.17
		(1.00)	(−0.20)		(1.15)	(0.20)		(1.20)	(0.05)	
8	$(^1D_2)6p[1]_{3/2}$	1.34	0.11	−0.01	0.52	0.32	0.02	1.23	0.30	−0.14
		(1.05)	(0.10)							
10	$(^1D_2)6p[3]_{5/2}$	1.72	0.19	0.00						
		(1.65)	(0.20)							
12	$(^1D_2)6p[3]_{7/2}$	1.75	0.21	0.02				0.39	0.54	−0.03
15	$(^1D_2)6p[2]_{3/2}$	1.50	−0.03	0.07	−0.11	0.19	0.01			

[a] The numbers in parentheses for peaks 5, 8, and 10 are from ref 12.

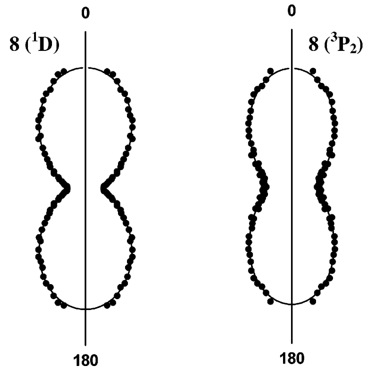

Figure 4. Two respresentative photoelectron angular distributions showing in the polar representation. The laser polarization is vertical. The dots are the experimental results for the final ion states $I^+(^1D)$ and $I^+(^3P_2)$, both for peak 8, and the solid lines are the corresponding fits using eq 5. The analyzed results are listed in Table 3.

partial waves for photoionization from *4f* states (peaks 3, 4, and 5). The observation of $k_{max} = 2$ for those peaks then suggests that the outgoing electrons via the *4f* intermediate state could be dominated by the *d*-wave character.

C. Autoionization Following Two-Photon Excitation of I ($^2P_{1/2}$). *1. Photoelectron Images.* As seen from Table 1, two-photon excitation of the spin−orbit excited state $I(^2P_{1/2})$ leads to autoionizing Rydberg series converging to the $^3P_1$ state of I^+. In contrast to the above (2 + 1) REMPI of $I(^2P_{3/2})$, the photoelectron images here, shown in Figure 5, are all characterized by a predominant single-ring feature. Those autoionizing states lie from 84 393 cm^{-1} to 88 676 cm^{-1} above the neutral ground state $I(^2P_{3/2})$. The IP of the I-atom is 84 312 cm^{-1}; thus, I^+ $^3P_2$ is the only energetically accessible final state, which accounts for the single-ring feature. Since the ion-core changes from $^3P_1$ to $^3P_2$, the observed autoionization processes must invoke the spin−orbit couplings of the $(^3P_1)np$ and $(^3P_1)nf$ autoionizing states with the $^3P_2$ continuum.

2. Autoionizing Dynamics. Since only the ion ground state $I^+(^3P_2)$ is energetically accessible, much of information on autoionization dynamics can only be retrieved from the photoelectron angular distribution. Listed in Table 4 are the Legendre coefficients β_{2k} obtained by the least-squares fits to observed distributions, and the corresponding angular distributions and the fits are shown as the polar representations in Figure 6. In contrast to the (2 + 1) REMPI process (Figure 4), a rich variety of angular distributions are noted. In general, for excitation of $I(^2P_{1/2})$ to an autoionizing state, k_{max} is equal to 2 due to the total number of photons involved in the process. From Table 4, β_2 ranges from −0.45 to 0.72, and β_4 is either close to zero or negative. Since the $I(^2P_{1/2})$ initial state is of spherical symmetry, a finite value of β_4 coefficients may reflect the alignment induced by two-photon absorption or from autoionization processes. Despite the observed perplexing distributions, a closer inspection of their general patterns reveals an interesting systematic. There are two types of general patterns: one type features distinct four-lobes along the diagonal directions, such as peaks 1, 2, 7, 13, 14, 19, 20, and 21, and the other is characterized by a near zero β_4 coefficient, thus showing either a pair of lobes (e.g., peaks 11, 16, and 17) or an oval shape (peaks 6, 9, and 18). Examining the assignments listed in Table 4 indicates that all *f*-type autoionizing states belong to the first type (with four-lobes), while all second types come from the *p*-type states. The only two exceptions are peaks 7 and 21, which are assigned to the *p*-series yet exhibit four-lobes features. It is particularly interesting to note that the four-lobe pattern of the peak 21 is of the most distinct among all of this work.

To comprehend the observed intriguing angular distributions will undoubtedly required high-level theoretical studies in the future. Nonetheless, it is instructive to use a simple model to gain some qualitative insights into the main observations. As aforementioned, the autoionization processes reported here must invoke the spin−orbit couplings of the ($^3P_1$-core) Rydberg states to the $^3P_2$ ion-continuum. Physically, it can arise from either the spin-flip in the core to release the Rydberg electron or the exchange interactions between the Rydberg and the core electrons.[20,28] Assuming that the interaction matrix for autoionization is of the Coulomb repulsive form[28]

$$V = \langle \Psi_i | e^2/r_{jk} | \Psi_n \rangle \tag{6}$$

where Ψ_n is the total wave function of the superexcited Rydberg state and Ψ_i the corresponding total wave function of the final ion state and the continuum electron. Treating it as a two-electron problem, for simplicity, only one term ($1/r_{12}$) is involved, which can be expanded as a sum over the spherical harmonics

$$\frac{1}{r_{12}} = \sum_{l=0}^{\infty} \frac{r_<^l}{r_>^{l+1}} Y_{lm}(r_1) Y_{l-m}(r_2) \tag{7}$$

and $r_<^l$ ($r_>^{l+1}$) is for the core (Rydberg) electron.[29]

The total wave functions can be expressed as products of core functions and outer electron functions

$$\Psi_n = \psi_{core}\psi_R \tag{8}$$

with ψ_{core} denoting the $^3P_1$-core; thus, $j = 1$ and

$$\Psi_i = \psi_i \psi_e \tag{9}$$

with ψ_i denoting the $^3P_2$ ion-continuum and $j = 2$.

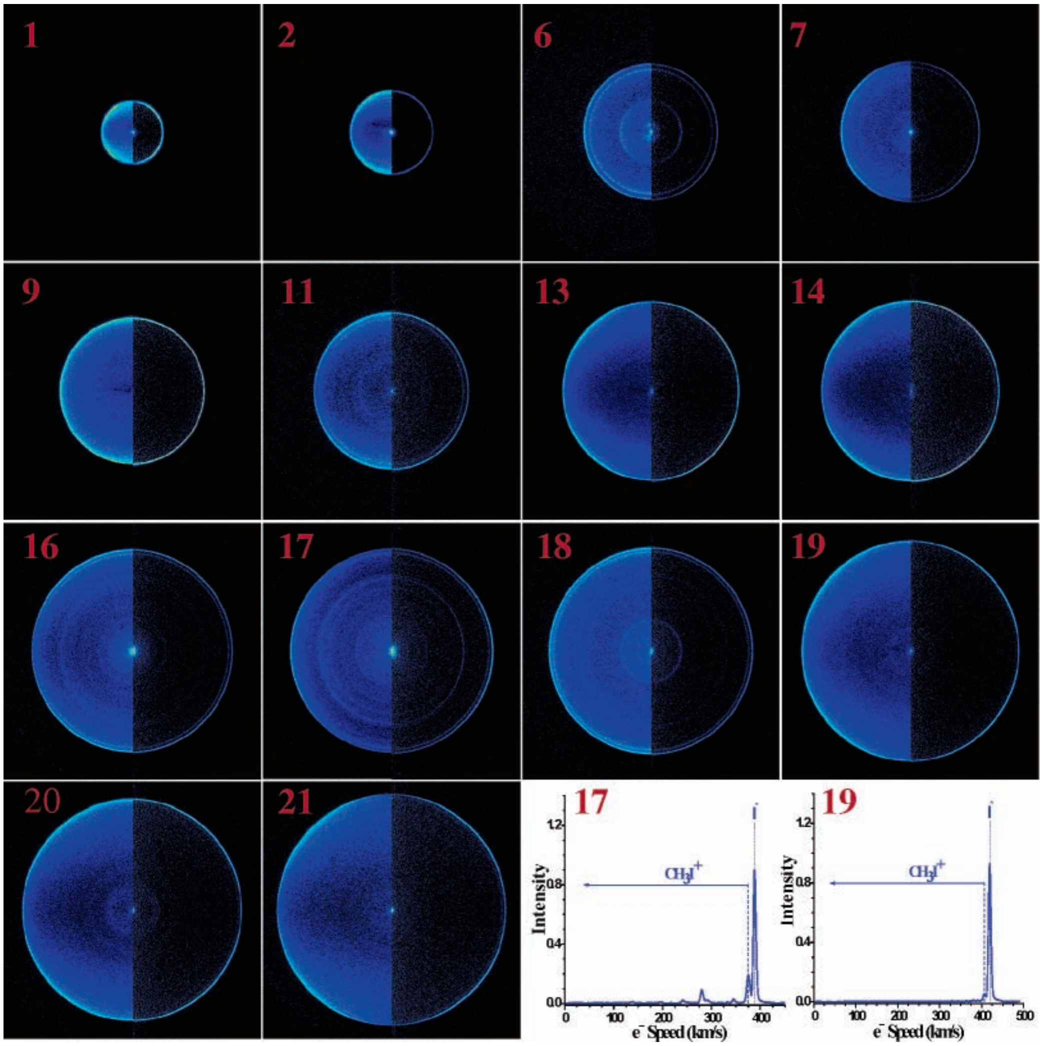

Figure 5. As Figure 3, but for the 14 autoionizing states originating from the I($^2P_{1/2}$) atom.

TABLE 4: Legendre Weighting Coefficients β_{2k} of Photoelectron Angular Distributions for Two-Photon Autoionizing Resonant Transitions from the Spin−Orbit Excited State I($^2P_{1/2}$)[a]

peak #	total energy (cm^{-1})	autoionization state	Legendre coefficients[b] β_2	β_4
1	84393.45	($^3P_1$)$4f[2]_{3/2,5/2}$	0.28 ± 0.10	−0.52 ± 0.05
2	84477.25	($^3P_1$)$4f[3]_{5/2}$	0.62 ± 0.06	−0.31 ± 0.06
6	85805.45	($^3P_1$)$8p[2]_{5/2}$	−0.21 ± 0.03	0.08 ± 0.06
7	85914.25	($^3P_1$)$8p[1]_{1/2}$	−0.28 ± 0.03	−0.32 ± 0.05
9	86031.95	($^3P_1$)$8p[1]_{3/2}$	0.17 ± 0.03	0.07 ± 0.03
11	86296.35	($^3P_1$)$8p[2]_{3/2}$	0.67 ± 0.03	−0.16 ± 0.05
13	86918.95	($^3P_1$)$5f[2]_{3/2,5/2}$	0.21 ± 0.04	−0.47 ± 0.03
14	86961.65	($^3P_1$)$5f[3]_{5/2}$	0.56 ± 0.04	−0.39 ± 0.03
16	87659.65	($^3P_1$)$9p[2]_{3/2}$	0.59 ± 0.06	−0.23 ± 0.05
17	87725.25	($^3P_1$)$9p[1]_{1/2}$	−0.45 ±0.03	0.06 ± 0.05
18	87784.05	($^3P_1$)$9p[0]_{1/2}$	0.15 ± 0.04	0.12 ± 0.03
19	88289.35	($^3P_1$)$6f[2]_{3/2,5/2}$	0.18 ± 0.05	−0.39 ± 0.04
20	80710.90	($^3P_1$)$6f[3]_{5/2}$	0.60 ± 0.04	−0.31 ± 0.04
21	88675.55	($^3P_1$)$10p[2]_{5/2}$	0.37 ± 0.03	−0.75 ± 0.06

[a] The final ion state is I$^+$($^3P_2$) for all peaks. [b] The uncertainty given here is ± one standard deviation from independent fittings of the four quadrants (see text for details).

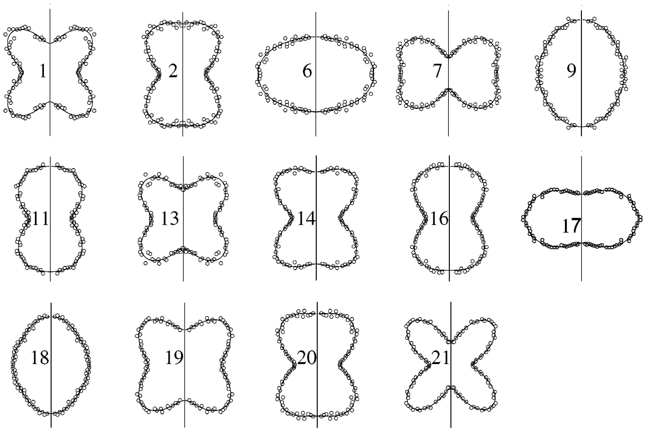

Figure 6. As Figure 4, but for the fourteen autoionizing states of this study. The autoionizing states originate from two-photon excitations of I($^2P_{1/2}$), and end with the same final ion state I$^+$($^3P_2$). Remarkably rich variations in photoelectron angular distributions are observed.

In the expansion of $1/r_{12}$, only three terms can couple $j = 1$ and 2, and they involve $l = 1$, 2, or 3.[28] Since the parity of the initial and final total wave functions, Ψ_n and Ψ_i, should be the same (conservation of parity), the matrix elements invoke $l =$ 1 and 3 (odd parity) must vanish. Hence, only the $l = 2$ term is at work, or

$$\frac{1}{r_{12}} = \frac{r_<^{\,2}}{r_>^{\,3}} Y_{2m}(r_1) Y_{2-m}(r_2) \tag{10}$$

And, eq 6 becomes

$$V = \left\langle \varphi_{\mathrm{i}}\varphi_{\mathrm{e}} \left| \frac{r_<^{\,2}}{r_>^{\,3}} Y_{2m}(r_1) Y_{2-m}(r_2) \right| \varphi_n \varphi_R \right\rangle \tag{11}$$

The ejection of an autoionization electron is mediated by the Coulombic interaction between the Rydberg electron and core electrons. Within the two-electron approximation, it can be shown that the angular part of this electron interaction involves a sum of Gaunt integrals[30] as

$$\sum_{m=-l}^{l} (-1)^m \langle Y_{l_{\mathrm{R}} m_{l\mathrm{R}}} | Y_{lm} | Y_{l_{\mathrm{e}} m_{l\mathrm{e}}} \rangle \tag{12}$$

where the index m's stands for the magnetic quantum number of the corresponding electron orbital angular momentum l's. The Gaunt integral can be expressed in terms of 3-j symbols[30]

$$\langle Y_{l_{\mathrm{R}} m_{l\mathrm{R}}} | Y_{lm} | Y_{l_{\mathrm{e}} m_{l\mathrm{e}}} \rangle = (-1)^m \left[\frac{(2l_{\mathrm{R}}+1)(2l+1)(2l_{\mathrm{e}}+1)}{4\pi} \right]^{1/2} \begin{pmatrix} l_{\mathrm{R}} & l_{\mathrm{e}} & l \\ m_{l\mathrm{R}} & m_{l\mathrm{e}} & m \end{pmatrix} \begin{pmatrix} l_{\mathrm{R}} & l_{\mathrm{e}} & l \\ 0 & 0 & 0 \end{pmatrix} \tag{13}$$

Thus, the Gaunt integral will be nonzero only under the following three conditions:

$$\begin{gathered} |l_{\mathrm{R}} + l_{\mathrm{e}}| \geq l \geq |l_{\mathrm{R}} - l_{\mathrm{e}}| \\ l_{\mathrm{R}} + l_{\mathrm{e}} + l = \text{even} \\ m_{l\mathrm{R}} + m_{l\mathrm{e}} = m \end{gathered} \tag{14}$$

As shown above, $l = 2$; hence, eq 14 leads to the propensity rule of $\Delta l = 0, \pm 2$ for autoionizing electrons. In the other words, for the p-like Rydberg states, $l_R = 1$; the allowed outgoing waves will be of the p- and f-types. As to the f-like Rydberg states, $l_R = 3$, the dominant autoionizing electrons, are likely the p- and f-waves again, though the contribution from the h-wave may not be neglected.

Examining the photoelectron angular distributions, as listed in Table 4 and shown in Figure 6, all six f-like autoionizing states display a "butterfly" shape, or a positive β_2 with a sizable negative β_4 value. The remaining eight p-series autoionizing states, except peaks 7 and 21, are characterized by near zero β_4 values. For both cases, the dominance of the usual autoionization propensity[20] of $\Delta l = 0$ prevails, namely, l-unchanging Rydberg-continuum transitions are distinctly more probable than l-changing autoionization processes. The observed variations in shapes could be attributed to different contributions from the two outgoing waves and their interferences, as well as the possible alignments effects. As to peaks 7 and 21, either the spectroscopic assignments to predominant p-type Rydberg states are in question or the autoionization processes invoke different mechanisms or couplings from the other p-series states to yield characteristic f-like outgoing electron waves. The above considerations are, of course, based on a single configuration in the J_cl coupling scheme. This assumption is expected to hold reasonably well for the $(^3P_1)$ core configuration of the Rydberg state. On the other hand, the final ion state $^3P_2$ might carry non-negligible $^1D_2$ characters from configuration interactions,[19] complicating the above simple arguments. Further theoretical studies are needed for a full account.

IV. Conclusions

A detailed study of the photoionization dynamics of the iodine atom was undertaken using photoelectron imaging technique. Two types of photoionization processes were identified and dynamics elucidated. For a (2 + 1) REMPI process, the ionization dynamics can be viewed, to a good approximation, as one-electron ejection process from the intermediate excited state, provided that the ion-core configuration is properly accounted for. On the other hand, the photoelectron angular distributions from autoionizing states exhibit rich and remarkable variations. A simple model is proposed to lay the foundation for a qualitative, physical insight into the main observations. Much more theoretical studies will be needed for deeper understandings of autoionizing electron angular distributions.

Acknowledgment. National Science Council of Taiwan supported this work under NSC 95-2119-M-001-002. We are indebted to Dr. C. Chang for the help in the initial phase of this project.

References and Notes

(1) For examples, Loo, R. O.; Haerri, H.-P.; Hall, G. E.; Houston, P. L. *J. Chem. Phys*. **1989**, *92*, 4222; Black, J. F.; Powis, I. *Chem. Phys*. **1988** *125*, 375; Chandler, D. W.; Janssen, M. H. M.; Stolte, M. S.; Strickland, R. N.; Thoman, J. W., Jr.; Parker, D. H. *J. Phys. Chem.* **1990**, *94*, 4839.

(2) Eppink, A. T. J. B.; Parker, D. H. *J. Chem. Phys.* **1999**, *110*, 832, and references therein.

(3) Johnson, B. R.; Kittrell, C.; Kelly, P. B.; Kinsey, J. L. *J. Phys. Chem.* **1996**, *100*, 7743, and references therein.

(4) Amamatsu, Y.; Yabushita, S.; Morokuma, K. *J. Chem. Phys.* **1996**, *104*, 9784, and references therein.

(5) Mulliken, R. S. *Phys. Rev.* **1942**, *61*, 277; Mulliken, R. S.; Teller, E. *Phys. Rev.* **1942**, *61*, 83.

(6) Fahr, A.; Nayak, A. K.; Kurylo, M. J. *Chem. Phys.* **1995**, *197*, 195.

(7) Zhong, D.; Cheng, P. Y.; Zewail, A. H. *J. Chem. Phys.* **1996**, *105*, 7864.

(8) Jiang, Y.; Giorgi-Arinazzi, M. R.; Bernstein, R. B. *Chem. Phys.* **1986**, *106*, 171.

(9) Pratt, S. T. *Phys. Rev. A* **1986**, *33*, 1718; *ibid* **1985**, *32*, 928.

(10) Pratt, S. T.; Dehmer, P. M.; Dehmer, J. L. *Chem. Phys., Lett.* **1986**, *126*, 12.

(11) Zhu, Y.; Grant, E. R. *J. Phys. Chem.* **1993**, *97*, 9582.

(12) Jung, Y.; Kim, Y. S.; Kang, W. K.; Jung, K. *J. Chem. Phys.* **1997**, *107*, 7187.

(13) Urban, B.; Bondybey, V. E. *J. Chem. Phys.* **2002**, *116*, 4938.

(14) Urban, B.; Bondybey, V. E. *Phys. Chem. Chem. Phys*. **2001**, *3*, 1942.

(15) Strobel, A.; Lochschmidt, A.; Fisher, I.; Schatteburg, G. N.; Bondybey, V. E. *J. Chem. Phys.* **1993**, *99*, 733.

(16) Strobel, A.; Fisher, I.; Lochschmidt, A.; Muller-Dethlefs, K.; Bondybey, V. E. *J. Phys. Chem.* **1994**, *98*, 2024.

(17) Lin, J. J.; Zhou, J.; Shiu, W. C.; Liu, K. *Rev. Sci. Instrum.* **2003**, *74*, 2495.

(18) Chang, C. S.; Luo, C. Y.; Liu, K. *J. Phys. Chem. A* **2005**, *109*, 1022.

(19) Minnhagen, L. *Ark. Fys.* **1962**, *21*, 415.

(20) Berkowitz, J. *Adv. Chem. Phys.* **1988**, *72*, 1.

(21) Dribinski, V.; Ossadtchi, A.; Mandelshtam, V. A.; Reisler, H. *Rev. Sci. Instrum.* **2002**, *73*, 2634.

(22) Huffman, R. E.; Larrabee, J. C.; Tanaka, Y. *J. Chem. Phys.* **1967**, *47*, 856.

(23) Moore, C. E. *Atomic Energy Levels*; Natl. Stand. Ref. Data Ser.; National Bureau of Standards: Washington, DC, 1971.

(24) Lambropoulos, P. *Adv. At. Mol. Phys.* **1976**, *12*, 87.

(25) Dixit, S. N.; Mckoy, V. C. *J. Chem. Phys.* **1985**, *82*, 3546.

(26) Suzuki, T.; Whitaker, B. J. *Int. Rev. Phys. Chem.* **2001**, *20*, 313.

(27) Appling, J. R.; White, M. G.; Kessler, W. J.; Fernandez, R.; Poliakoff, E. D. *J. Chem. Phys.* **1988**, *88*, 2300.

(28) Berkowitz, J. *Photoabsorption, Photoionization and Photoelectron Spectroscopy*; Academic: New York, 1979.

(29) Zare, R. N. *Angular Momentum*; John Wiley & Sons, Inc.: New York, 1988.

(30) Thompson, W. J. *Angular Momentum*; John Wiley & Sons, Inc.: New York, 1994.